Case Studies in Thermal Engineering 79 (2026) 107820

Contents lists available at ScienceDirect

Case Studies in Thermal Engineering

journal homepage: www.elsevier.com/locate/csite

Metal-foam skeleton effects on PCM thermal storage for greenhouse microclimate control: A numerical study

Samir Gouga [a,b], Atef Chibani [a,***], Kamel Mesmoudi [q,r], Farhan Lafta Rashid [c], Zaki Mrzog Alaofi [d], Yazen M. Alawaideh [e,*], Tasneem Alayed [f], Mohamed kezzar [g], Mohamed Rafik Sari [h], Ibrahim Mahariq [i,j,k,l,m,**], Aya M. Al-Zuheiri [n], Ioan-Lucian Popa [o,p]

[a] *Research Center in Industrial Technologies CRTI, P.O. Box 64, Cheraga, 16014, Algiers, Algeria*
[b] *Applied Physic Energetic laboratory (L.P.E.A), Physics Department, Faculty of Matter Science, University of Batna 1, Avenue Boukhlouf Mohamed El Hadi, 05000, Batna, Algeria*
[c] *Petroleum Engineering Department, College of Engineering, University of Kerbala, Karbala, 56001, Iraq*
[d] *Department of Mathematics, Applied College at Mahail Aseer, King Khalid University, Saudi Arabia*
[e] *MEU Research Unit, Middle East University, Amman, Jordan*
[f] *Department of Basic Sciences / Scientific, Faculty of Science, Applied Science Private University, Jordan*
[g] *Materials and Energy Engineering Laboratory (LMGE), Technology Department, Faculty of Technology, 20 Aout 1955 University of Skikda, PO Box 26, 21000, Skikda, Algeria*
[h] *Mechanics of Materials and Plant Maintenance Research Laboratory (LR3MI), Faculty of Technology, Badji Mokhtar-Annaba University, PO Box 12, Annaba, 23000, Algeria*
[i] *College of Engineering and Architecture, Gulf University for Science and Technology, Mishref, Kuwait*
[j] *Najjad Zeenni Faculty of Engineering, Al-Quds University, Jerusalem, Palestine*
[k] *Department of Electrical and Electronic Engineering, Faculty of Engineering and Architecture, Istanbul Gelisim University, Avcılar, Istanbul, 34310, Istanbul, Türkiye*
[l] *Department of Medical Research, China Medical University Hospital, China Medical University, Taichung, Taiwan*
[m] *University College, Korea University, Seoul, 02481, South Korea*
[n] *Department of Basic Sciences, Middle East University, Amman, 11831, Jordan*
[o] *Department of Computing, Mathematics and Electronics, "1 Decembrie 1918" University of Alba Iulia, 15 510009, Alba Iulia, Romania*
[p] *Faculty of Mathematics and Computer Science, Transilvania University of Brasov, Iluiu Maniu Streat 50, 5000917, Romania*
[q] *Department of Agronomy, University of Batna 1, Alleys of 19 May, 05000, Batna, Algeria*
[r] *Laboratoire de Mécanique des Structures et Matériaux, Université Batna 2, Avenue Chahid Boukhlouf 05000, Batna, Algeria*

* Corresponding author.
** Corresponding author. College of Engineering and Architecture, Gulf University for Science and Technology, Mishref, Kuwait.
*** Corresponding author.

E-mail addresses: sgouga.8226@gmail.com (S. Gouga), chibaniatef@gmail.com (A. Chibani), kamelagro@hotmail.fr (K. Mesmoudi), farhan.lefta@uokerbala.edu.iq (F.L. Rashid), zaleawfi@kku.edu.sa (Z.M. Alaofi), yazen_awaida@yahoo.com (Y.M. Alawaideh), t_ibrahim@asu.edu.jo (T. Alayed), kezzar_m@yahoo.com (M. kezzar), mohamed-rafik.sari@univ-annaba.dz (M.R. Sari), ibmahariq@gmail.com (I. Mahariq), alzuheiri@meu.edu.jo (A.M. Al-Zuheiri), lucian.popa@uab.ro (I.-L. Popa).

https://doi.org/10.1016/j.csite.2026.107820
Received 1 November 2025; Received in revised form 21 January 2026; Accepted 11 February 2026
Available online 12 February 2026
2214-157X/

G R A P H I C A L A B S T R A C T

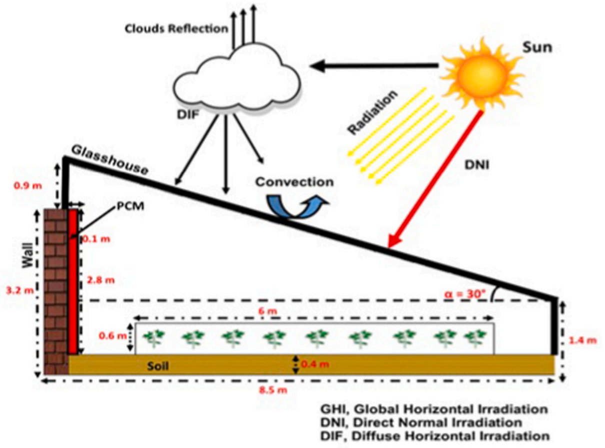

A R T I C L E I N F O

Keywords:
Greenhouse microclimate
CFD simulations
Phase change materials (PCMs)
Thermal regulation
Metal foam

A B S T R A C T

This study investigates passive thermal management strategies for a south-facing greenhouse operating under hot-arid diurnal conditions by integrating phase change materials (PCMs) into the north wall and enhancing their thermal response using open-cell metal foams. A 2D transient CFD microclimate model is developed in ANSYS Fluent. The impact of metal-foam (MF) type is examined by comparing copper, aluminum, and steel foams at 20 PPI and high porosity (ε = 0.93). Results show that inserting MF improves heat spreading inside the PCM modules, leading to smoother temperature fields, reduced local overheating during charging, and more effective latent-heat utilization. Among the tested foams, copper provides the strongest stabilization, typically lowering PCM daytime peak or plateau temperatures by about 5–7 K relative to the no-foam case, followed by aluminum (about 3–5 K) and steel (about 2–3 K). Foam enhancement also accelerates melting, increasing the maximum daily liquid fraction from about 0.22 (no foam) to about 0.35 (copper), 0.33 (aluminum), and 0.29 (steel). The improved thermal coupling modifies buoyancy forcing and airflow patterns, reducing stagnant zones and promoting more uniform circulation. These findings provide material-level guidance for designing MF–PCM storage modules to improve greenhouse temperature buffering with minimal energy input.

Nomenclatures

Latin symbol		
A_{mush}	Mushy-zone constant	$kg{\cdot}m^{-3}{\cdot}s^{-1}$
c_j	Species mass fraction of component j	–
cp	Specific heat at constant pressure	$J{\cdot}kg^{-1}{\cdot}K^{-1}$
C_f	Forchheimer inertial coefficient	m^{-1}
d_l	Foam ligament (fiber) diameter	m
dp	Average particle diameter	m
D_j	Diffusion coefficient of component j	$m^2{\cdot}s^{-1}$
f	Liquid fraction	–
g	Gravitational acceleration	$m{\cdot}s^{-2}$
H	Total enthalpy	$J{\cdot}kg^{-1}$
h	Sensible enthalpy	$J{\cdot}kg^{-1}$
I	Radiative intensity	$W{\cdot}m^{-2}{\cdot}sr^{-1}$
I_f	Radiative intensity after film transmission	$W{\cdot}m^{-2}{\cdot}sr^{-1}$
L	Latent heat of phase change	$J{\cdot}kg^{-1}$
L_m	Macroscopic length	m
K	Permeability	(m^2)
k	hermal conductivity	$W{\cdot}m^{-1}{\cdot}K^{-1}$)
P	Pressure	Pa
S	Momentum source term	$N{\cdot}m^{-3}$

(*continued on next page*)

(*continued*)

Latin symbol		
S_i	Momentum source term in direction i	$N \cdot m^{-3}$
S_a	Volumetric mass source	$kg \cdot m^{-3} \cdot s^{-1}$
S_Φ	Source term of transported quantity	—
T	Temperature	K
$T_{solidus}$	Solidus temperature	K
$T_{liquidus}$	Liquidus temperature	K
t	Time	s
$\vec{v}$	Fluid velocity vector	$m \cdot s^{-1}$
v_i	Velocity component in direction i	$m \cdot s^{-1}$
x, y, z	Cartesian coordinates	m
Greek symbols		
α	Permeability	m^2
β	Small number	–
ε	Porosity	–
κ_f	Short-wave extinction (absorption) coefficient	m^{-1}
λ	Thermal conductivity	$W \cdot m^{-1} \cdot K^{-1}$
μ	Dynamic viscosity	Pa·s
ρ	Fluid density	$kg \cdot m^{-3}$
Φ	Generic transported quantity	–
Γ_Φ	Effective diffusivity	$m^2 \cdot s^{-1}$
Subscripts/superscripts		
PCM	Phase-change material	
ref	Reference	
s	Solid	
ℓ	Liquid	
Ref	reference	

1. Introduction

Population growth, climate change, and increasing pressure on food security have accelerated global efforts toward sustainable and resource-efficient agriculture [1]. Greenhouses enable year-round cultivation by providing a controlled microclimate, which is especially valuable in regions exposed to harsh or highly variable outdoor conditions [2]. However, maintaining suitable temperature and humidity often requires substantial heating and cooling energy, leading to high operating costs and non-negligible environmental impacts [3,4].

In response, recent research has increasingly targeted energy-efficient greenhouse systems capable of maintaining favorable microclimates with minimal resource consumption [5,6]. Effective thermal regulation is particularly critical in extreme and strongly diurnal climates, where temperature stability directly influences crop productivity and operating costs [7]. Among passive thermal-management options, phase change materials (PCMs) have gained considerable attention for greenhouse applications [8,9]. Through latent heat absorption and release during melting and solidification, PCMs can attenuate indoor temperature swings and shift thermal peaks, thereby reducing reliance on active heating and cooling systems [10].

PCMs have been widely investigated as passive or hybrid thermal buffers in greenhouses [11], with implementations ranging from north-wall storage layers and PCM-enhanced bricks/coatings to ceiling panels and root-zone modules. A recurring outcome is the attenuation of diurnal indoor temperature variability, alongside higher nighttime temperatures and reduced dependence on auxiliary heating/cooling, although the magnitude of improvement depends strongly on design and operating conditions [12,13]. Embedding salt-hydrate composite PCMs within porous brick matrices has been reported to improve wall thermal buffering and insulation compared with conventional construction [14]. PCM-based storage units have also been experimentally shown to maintain the greenhouse warmer after midnight (reported differences spanning roughly 1–8 °C in winter conditions), and data-driven tools have been used to predict indoor temperature and support control-oriented operation toward low-energy greenhouses [15]. For root-zone applications, an optimal PCM melting temperature near 15 °C has been identified, with macro-encapsulation improving effectiveness. However, PCMs may reduce heater runtime rather than fully replacing nighttime heating, and economic feasibility remains sensitive to PCM cost (for example, around 8 €/kg in one assessment) [16].

Energy savings reported across climates and crops commonly fall in the range of about 19–33%, with stronger benefits under larger day–night temperature differences; hydrated salts tend to perform best when their phase-change temperature is about 3–4 °C above the minimum temperature setpoint [17]. Because the low thermal conductivity of many PCMs can limit charging/discharging rates, heat-transfer enhancement strategies have been proposed, including coupling PCM layers with conductive inserts, where near-doubling of stored and released energy has been reported (e.g., 9.67 to 18.89 MJ/m^3 storage and 8.95 to 17.58 MJ/m^3 release), leading to improved nighttime thermal support [18]. Parametric optimization studies further indicate that selecting appropriate PCM melting temperature and thickness is critical where configurations using a melting point near 15 °C and thickness around 4 cm have been reported to maximize the duration of crop-suitable indoor conditions [19]. Form-stable and photothermal composite PCMs have shown high solar-to-thermal conversion (above 88%) and measurable improvements in greenhouse buffering performance, including extending the period during which indoor air remains above 20 °C [20]. Finally, simulations highlight that PCM location, orientation, and integration with operational measures (e.g., thermal screens) can significantly affect heating demand and yield outcomes [21], while reviews consistently conclude that PCMs can reduce temperature swings and shift peaks, provided that the integration strategy is tailored to the greenhouse design and climate [12,13].

PCMs can stabilize greenhouse temperatures, but their low thermal conductivity (0.2–0.6 W m^{-1} K^{-1}) slows melting/solidification and creates internal temperature gradients. A practical solution is to embed metal foams, whose interconnected ligaments greatly enhance heat spreading and can raise the composite effective conductivity to the order of 10^2 W m^{-1} K^{-1} [22–24]. This improves daytime charging, reduces stratification, increases peak-temperature shaving, and supports a longer, smoother nighttime heat release. A recent transient CFD study examined a glass-roofed greenhouse using a copper-foam/PCM layer, considering four PCMs, pore density, airflow behavior, and outdoor wind effects [25]. The key finding was that PCM selection largely controls the microclimate response (daytime peak reduction versus pre-dawn support), whereas pore-density changes have only a minor impact on bulk temperatures, mainly shifting charging/discharge timing.

In this context, the present work quantifies how the metal-foam skeleton material (copper, aluminum, or steel) affects the charging and discharging behavior of PCM storage modules and, consequently, the greenhouse microclimate. Prior greenhouse studies have primarily emphasized PCM selection, placement, thickness, or pore-density effects, whereas the influence of the foam skeleton material has rarely been isolated and assessed under identical geometric and operating conditions. To address this gap, a validated 2D transient CFD microclimate model is implemented in ANSYS Fluent for a south-facing greenhouse subjected to hot-arid diurnal forcing, with PCMs integrated into the north wall and enhanced using open-cell metal foams. Copper, aluminum, and steel foams are compared at fixed morphology (20 PPI) and high porosity ($\varepsilon = 0.93$), enabling a strictly material-level comparison. The novelty lies in establishing a direct link between foam material properties and the coupled thermal and flow-field responses, including temperature homogenization and peak reduction during charging, latent-heat utilization through melting/solidification, and buoyancy-driven circulation patterns and stagnant-zone mitigation. These outcomes provide practical guidance for selecting foam materials in MF–PCM greenhouse storage modules aimed at passive temperature buffering with minimal energy input.

2. Physical model

A two-dimensional cross-section is used to represent a south-facing greenhouse, as shown in Fig. 1. The enclosure is 8.5 m long, with a 3.2 m north-wall height, a 1.4 m south eave, and a roof inclination of about 30°. The north wall is modeled as an ash-brick structure (0.40 m thick) coupled to a PCM storage layer (0.10 m), while the roof/cover is treated as a semi-translucent envelope for solar transmission. The interior domain includes a soil layer (0.40 m thick) and a crop-canopy region (approximately 0.60 m high), both represented as porous media to account for aerodynamic resistance and heat exchange with the greenhouse air. Solar forcing is prescribed as direct and diffuse irradiation transmitted through the cover and absorbed by the soil, canopy, and wall surfaces. Heat losses to the outdoor environment are captured through wind-driven convection and long-wave radiation exchange with the sky. Inside the enclosure, surface-to-surface long-wave radiation and buoyancy-induced circulation govern the transient airflow and temperature distribution. During daytime, heating of the cover and soil generates rising plumes, whereas the shaded north wall

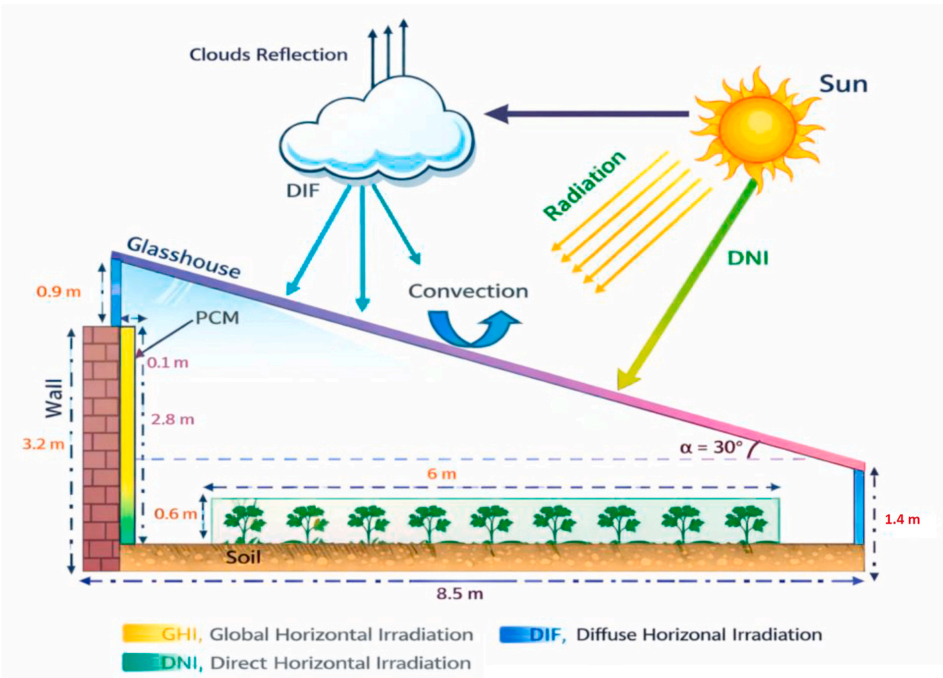

Fig. 1. Section view of the greenhouse with PCM–copper-foam wall.

remains comparatively cooler; after sunset, latent-heat storage moderates indoor cooling and modifies the circulation pattern.

Thermal storage is implemented by integrating organic PCM panels into the north wall and supplementing them with supercooled salt-hydrate units embedded in open-cell metal foams (copper, aluminum, and steel). The foam matrices increase the effective thermal conductivity and interfacial area, thereby accelerating charging and discharging and improving the thermal response of the storage modules. To characterize the transient microclimate, temperature is monitored at 22 locations distributed across the indoor air, crop canopy, soil, PCM regions, and the ash-brick wall, as depicted in Fig. 2. Representative horizontal and vertical transects (Lines 1–4 in Fig. 2) are also used to extract airflow and thermal fields. Envelope-material properties are listed in Table 1, PCM and metal-foam properties are summarized in Table 2, and monitoring-point coordinates are given in Table 3.

3. Mathematical modeling

3.1. Conventional greenhouse model without PCMs

Variations in ambient temperature and solar irradiation induce unsteady changes in the greenhouse air temperature and humidity. To capture these coupled dynamics, a two-dimensional transient CFD microclimate model is developed. The framework combines (1) porous-media representations for soil and crop canopy, (2) a turbulence closure for indoor airflow, (3) radiative transfer for solar gains through the cover, and (4) species transport to resolve water-vapor distribution [26].

3.1.1. Porous media model for soil and crop canopy

The soil layer and the crop canopy are modeled as porous zones that impose momentum losses on the airflow. These losses are introduced as a sink term in the momentum equation using a Darcy–Forchheimer formulation [27,28]:

$$S_i = -\left(\frac{\mu}{\alpha}\nu_i + C_2\frac{1}{2}\rho\ |\nu|\nu_i\right) \tag{1}$$

where S_i is the momentum source term in the i-direction, μ is the dynamic viscosity, $1/\alpha$ is the viscous resistance coefficient, ϑ_i is the velocity in the i direction, ρ is the fluid density, and C_2 is the inertial resistance coefficient. Since the fluid flow inside the soil or crop canopy is laminar, the Blake-Kozeny equation is used to calculate the inertial resistance coefficient [38]:

$$\frac{|\Delta p|}{L_m} = \frac{150\,\mu}{d_p^2}\ \frac{(1-\varepsilon)^2}{\varepsilon^3}\ \nu_\infty \tag{2}$$

Here, p represents the pressure, L_m is the length along the macroscopic pressure gradient in porous media, d_p denotes the average particle diameter, ε is the porosity, and ν_∞ stands for the superficial (volume-averaged) velocity. Based on the Ergun equation [38], the following relationships can be derived:

$$\frac{1}{\alpha} = \frac{150}{d_p^2}\ \frac{(1-\varepsilon)^2}{\varepsilon^3}, \tag{3}$$

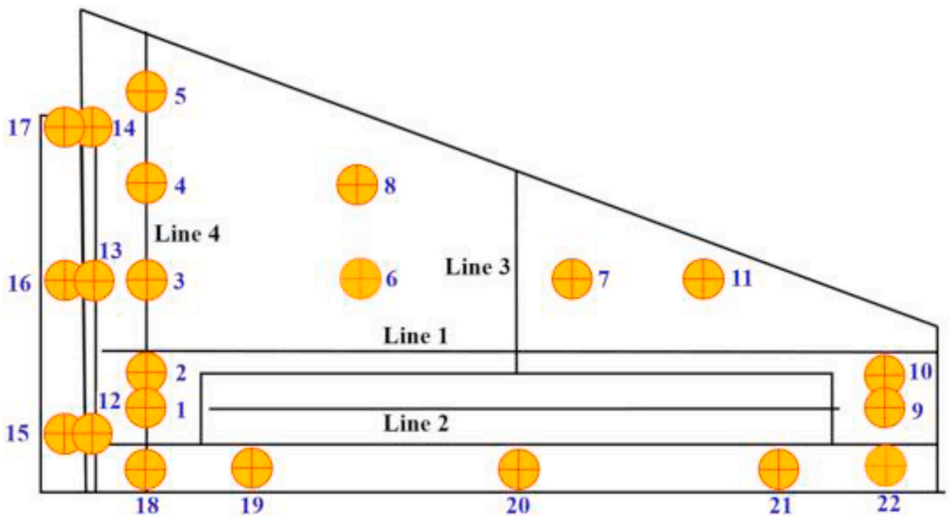

Fig. 2. Schematic of sensor positions and analysis lines within the greenhouse.

Table 1
Thermophysical properties of greenhouse envelope materials [25].

Material	Density ($kg{\cdot}m^{-3}$)	Thermal conductivity ($W{\cdot}m^{-1}{\cdot}K^{-1}$)	Specific heat capacity ($J{\cdot}kg^{-1}{\cdot}K^{-1}$)	Thickness (mm)	Absorptivity (α)
Air	1.205	0.02	1013	-	-
Ground	1300	1.00	800	400	0.95
Canopy	700	0.17	2310	600	0.46
Glass	840	0.76	2700	4	UV; 0.05/PAR; 0.1/NIR; 0.2
Ash brick	989	0.81	1700	400	-

Table 2
Thermophysical properties of copper foam and selected PCMs [25].

Material	ρ (Kgm^{-3})	k ($W{\cdot}m^{-1}{\cdot}K^{-1}$)	C_p ($JKg^{-1}\ K^{-1}$)	Latent heat ($kJkg^{-1}$)	Melting temperature (°C)
$KF4H_2O$	1450	0.56	2200	200	18
RT25	770	0.2	2000	180	25-26
Copper	8933	350-401	381	-	-
Aluminum	2719	202.4	871	-	
Steel	7830	13	468	-	-

Table 3
Spatial coordinates of monitoring points used for temperature measurements.

Zone	Point	X (m)	Y (m)
Greenhouse (Air/Crop Zone)	1	0.95	0.70
	2	0.95	1.00
	3	0.95	1.80
	4	0.95	2.60
	5	0.95	3.40
	6	2.95	1.80
	7	4.95	1.80
	8	2.60	2.95
	9	7.90	0.70
	10	7.90	1.00
	11	6.20	1.80
PCM Zone	12	0.45	0.50
	13	0.45	1.80
	14	0.45	3.10
Ash Brick Zone	15	0.20	0.50
	16	0.20	1.80
	17	0.20	3.10
Ground (Soil Zone)	18	0.95	0.20
	19	1.95	0.20
	20	4.45	0.20
	21	6.90	0.20
	22	7.90	0.20

$$C_2 = \frac{3.5}{d_p}\ \frac{(1-\varepsilon)}{\varepsilon^2} \tag{4}$$

3.1.2. Turbulence model for air

The soil and crop canopy are represented as anisotropic porous media with uniform properties. The porous resistance is incorporated into the momentum equation via a source term comprising viscous and inertial components, as defined in Eq. (1). The corresponding resistance coefficients are derived from the Blake–Kozeny relation and the Ergun equation using the following input parameters:

- **Soil:** porosity = 0.45, equivalent particle diameter = 3.0×10^{-3} m

Table 4
Porous-media parameters used for the soil and crop canopy.

Medium	Porosity ε	Characteristic Length, $\mathbf{d_p}$ (m)	α (m^{-2})	C_2 (m^{-1})
Soil	0.45	3.0×10^{-3}	1.6×10^{6}	420
Crop canopy	0.75	1.2×10^{-2}	2.3×10^{5}	95

- **Crop canopy:** porosity = 0.75, equivalent particle diameter = 1.2×10^{-2} m

These parameter values, consistent with the porous-media modeling framework for greenhouse applications [28], yield the viscous and inertial resistance coefficients listed in Table 4. The parameters are consistent with those employed in prior CFD studies of greenhouse environments and provide a physically realistic representation of airflow resistance through soil and vegetation. The porous media model for soil and crop canopy incorporates momentum sink terms to account for airflow resistance, following the formulation employed in greenhouse CFD simulations [28]. The source term in the momentum equation includes both viscous and inertial components as defined in Eq. (1). While the specific parameter values in Table 1 reflect the physical properties of the media in this study, the modeling approach is consistent with established methodologies for representing vegetative and soil resistance in agricultural CFD applications.

The simulation employed the Renormalization Group (RNG) k-ε turbulence model [29,30], which enhances precision by incorporating an extra term to account for fluid viscosity in low Reynolds number flows [28,31,32]. The governing equation for the RNG model is given by

$$\frac{\partial(\rho\Phi)}{\partial t} + \mathrm{div}(\rho\vec{v}\Phi) = \mathrm{div}\,(\Gamma_\Phi\ \mathrm{grad}\Phi) + S_\Phi, \tag{5}$$

Here, Φ represents the quantity (temperature or relative humidity). Γ_Φ is the diffusion coefficient of Φ, assumed constant, and S_Φ is a source term.

3.1.3. Solar radiation model

Solar radiation is the primary heat source. The semi translucent cover absorbs, reflects, and transmits incoming short-wave irradiation. Directional effects are modeled with the Discrete Ordinates (DO) method, along each discrete ray, the radiative transfer equation is written as [28]:

$$\frac{dI(\vec{r},\vec{s})}{ds} + K_f\ .I(\vec{r},\vec{s}) = K_f\ .\ I_f, \tag{6}$$

where $\vec{r}$ represents the direction vector, $\vec{s}$ is the position vector, K_f denotes the film's absorptivity, I is the solar radiation intensity, and I_f indicates the intensity of radiation transmitted through the film.

3.1.4. Species transport for water vapor

Humidity transport is modeled by solving a conservation equation for water vapor in the air–vapor mixture [28]:

$$\frac{\partial}{\partial t}(\rho c_j) + \mathrm{div}\,(\rho\vec{v}c_j) = \mathrm{div}\,(D_j\mathrm{grad}(\rho c_j)) + S_a \tag{7}$$

where c_j is the volumetric concentration of component j in the mixed gas, D_j is the diffusion coefficient of the component, and S_a is the additional generalized source.

3.2. Greenhouse model with organic PCM on north wall and additional supercooled salt hydrate units

In addition to the airflow, radiation, porous-media, and species-transport models, the PCM-equipped greenhouse requires a phase-change model. The organic PCM integrated into the north wall and the supercooled salt-hydrate units are simulated using the enthalpy–porosity method, in which the phase change is tracked through the local liquid fraction f [33]:

$$f = \begin{cases} 0 & T < T_{solidus,} \\ \dfrac{T - T_{solidus}}{T_{liquidus} - T_{solidus}} & T_{solidus} < T < T_{liquidus,} \\ 1 & T > T_{liquidus,} \end{cases} \tag{8}$$

where $T_{solidus}$ and $T_{liquidus}$ are the solidus and liquidus temperature. When $0 < f < 1$, the PCM is in the mushy zone and is treated as a porous medium that damps the velocity field.

To simplify the phase-change heat transfer model, the following assumptions are adopted:

- PCM thermophysical properties are constant within each phase.
- The liquid PCM is Newtonian and incompressible.
- Surface-tension effects and volume-change-induced motion are neglected; enthalpy varies linearly within the phase-change interval.
- Container shells for the organic PCM and salt-hydrate units are thin enough to be it neglected.
- Thermal contact resistance between wall layers is neglected. A sensitivity test for the best-performing copper-foam configuration using Rc = 0 to 1×10^{-4} m^2 K W^{-1} showed changes below 0.3 K in average indoor temperature and below 2% in daily fluctuation reduction, indicating that interfacial resistance is secondary at the system scale considered here.

The governing equations for the PCM region are [25,33]:

Continuity equation:

$$\frac{\partial \rho_{\text{PCM}}}{\partial t} + \nabla(\rho_{PCM}\vec{\nu}) = 0, \tag{9}$$

Momentum equation:

$$\frac{\partial \rho_{\text{PCM}}}{\partial t} + \nabla(\rho_{\text{PCM}}\vec{\nu}\,\vec{\nu}) = -\nabla P + \nabla(\mu\,\vec{\nu}\,) + \rho_{\text{PCM}}\,\vec{g} + S, \tag{10}$$

Energy equation:

$$\frac{\partial(\rho_{\text{PCM}}H)}{\partial t} + \nabla(\rho_{\text{PCM}}\vec{\nu}\,H) = \lambda\,\nabla^2 T, \tag{11}$$

Where the total enthalpy is:

$$H = h + fL, \tag{12}$$

$$h = h_{\text{ref}} + \int_{T_{\text{ref}}}^{T} c_p dT, \tag{13}$$

The mushy-zone momentum sink is:

$$S = \frac{(1-f)^2}{f^3 + \beta} A_{\text{mush}}\vec{\nu}, \tag{14}$$

where β set to 10^{-4} prevents division by zero and $A_{\text{mush}} = 10^5$ is the mushy zone constant.

3.3. PCM–metal-foam model

The PCM–metal-foam insert on the north wall is treated as a porous PCM–foam composite under the local thermal equilibrium (LTE) assumption, meaning the foam and PCM share a common temperature field. The validity of LTE was checked by running a two-temperature (LTNE) formulation; the predicted foam–PCM temperature difference, liquid fraction, enthalpy, and velocity fields are essentially unchanged at the present grid and time-step resolution. This behavior is expected because the foam's large interfacial area and high conductivity promote rapid interphase heat exchange. Therefore, the energy equation is solved in a single-temperature form (Eq. (11)) using mixture-effective thermophysical properties, while the momentum equation in the liquid/mushy PCM is augmented by a porous resistance term representing the foam. Within the PCM–foam region, a Darcy–Forchheimer momentum sink is introduced [25]:

$$\mathrm{S\_(MF)} = \left(\frac{\mu}{K} + \rho C_f v\left|v\right|\right) \tag{15}$$

where K is permeability and Cf is the inertial (Forchheimer) coefficient and can be expressed as:

$$\mathrm{C\_(f)} = 0.00212(1-\varepsilon)^{-0.132}\left(\frac{dl}{dp}\right)^{-1.63} \tag{16}$$

$$\frac{K}{d_p^2} = 0.00073(1-\varepsilon)^{-0.224}\left(\frac{dl}{dp}\right)^{-1.11} \tag{17}$$

with the ligament-to-pore diameter ratio

$$\frac{dl}{dp} = 1.18\int\frac{1-\varepsilon}{3\pi}\left(\frac{1}{1-e^{(1-\varepsilon)/0.04}}\right), \mathrm{d_p} = \frac{0.0254}{PPI} \tag{18}$$

The mixture heat capacity and thermal conductivity are:

$$k_{eff} = (1-\varepsilon)k_{MF} + \varepsilon k_{PCM} \tag{19}$$

$$(\rho Cp)_{eff} = (1-\varepsilon)\,(\rho Cp)_{MF} + \varepsilon(\rho Cp)_{PCM} \tag{20}$$

3.4. Boundary conditions

In all configurations, the soil and crop canopy are modeled as porous media, and porous-jump boundary conditions are applied at their interfaces with the airflow domain. The PO cover is treated as a semi-translucent medium, whereas the remaining enclosure surfaces are specified as solid walls. On the exterior sides of the north wall, north roof, and PO film, a combined heat-transfer boundary condition is imposed, accounting for convection to the ambient air ($h = 10$ W m^{-2} K^{-1}) and long-wave radiation (emissivity $\varepsilon = 0.93$). The short-wave absorptivities are set to 0.8 for the north wall and roof and to 0.05 for the PO film. Conjugate heat transfer is enforced at the internal wall surfaces and at the surfaces of the supercooled salt-hydrate units to ensure consistent heat flux and temperature continuity. The east and west walls are assumed adiabatic, and the lateral and bottom boundaries of the soil are also taken as thermally insulated.

Transient simulations are performed using time-dependent external forcing based on hourly ambient temperature and solar radiation intensity. These profiles are applied to the greenhouse envelope to represent the diurnal evolution of meteorological conditions. The imposed hourly values are listed in Table 5. *Ambient temperature* follows a representative hot-arid daily cycle, varying from about 289 K at night to a peak of 318 K during the day, while solar irradiation rises from zero at night to a maximum of approximately 850 W m^{-2} near solar noon. In the CFD solver, both inputs are implemented via piecewise-linear interpolation between consecutive hourly values to provide smooth temporal variation and maintain numerical stability. Reporting the complete forcing profiles improves transparency and enables reproducibility of the numerical setup.

4. Numerical method

The governing equations and boundary conditions are solved in ANSYS Fluent using a 2D, transient, pressure-based implicit solver. Pressure–velocity coupling is treated with the SIMPLEC algorithm. Pressure is discretized using the PRESTO scheme, while the momentum, energy, and species equations are discretized with a second-order upwind scheme. The turbulent kinetic energy and dissipation-rate equations, as well as the Discrete Ordinates (DO) radiation equation, are discretized using a first-order upwind scheme to improve robustness. Convergence at each time step is ensured by imposing residual tolerances of 10^{-6} for the energy and DO equations and 10^{-3} for continuity, momentum, and species transport.

A non-uniform mesh is adopted (Fig. 3), with local refinement near the roof/cover, the north-wall PCM/thermal-storage region, and the soil–canopy interfaces to resolve buoyancy-driven boundary layers, radiative heat exchange, and steep temperature gradients during PCM charging and discharging. Mesh sensitivity is first assessed by comparing three grid resolutions (47,786, 161,451, and 286,516 cells). The predicted average-temperature evolution obtained with the medium and fine meshes is nearly identical over the full transient cycle, whereas the coarsest mesh exhibits small deviations, particularly during periods of strong thermal gradients. Based on this convergence behavior, the 161,451-cell mesh is selected as a suitable compromise between accuracy and computational cost and is used for all subsequent simulations. Time-step sensitivity is then evaluated using $\Delta t = 2.5$, 5, and 7.5 s. The resulting temperature trajectories show negligible differences, indicating weak dependence on temporal discretization within this range. Consequently, a time step of 5 s is adopted to ensure stable convergence while maintaining reasonable computational effort (see Fig. 4).

The present model is validated against the greenhouse measurements reported in Ref. [34], where a root-zone thermal environment control system based on a latent heat functional thermal fluid isimplemented and tested under realistic operating conditions. In that work, the authors monitored the greenhouse thermal response over a full day, providing a suitable benchmark for assessing whether the present framework can reproduce the coupled, diurnal heating–cooling dynamics driven by solar forcing and ambient variations. Fig. 5 compares the experimental temperature evolution from Ref. [34] with the present transient prediction (ANSYS Fluent). The model captures the overall diurnal trend well, including the rapid rise during the daytime heating period, the subsequent cooling phase, and the timing of the temperature extrema. Quantitatively, the deviation remains small over most of the cycle, with a minimum relative error of about 0.1%, while the largest discrepancy reaches approximately 7% and is confined to short intervals around the steepest transients (near the peak and the rapid post-peak drop). Such localized differences are expected because the experimental greenhouse involves additional thermal and control effects (e.g., root-zone heat exchange, moisture-related processes, and operational variability) that are simplified in the CFD representation, and because uncertainties in meteorological inputs and envelope properties can amplify mismatch during periods of strong gradients. Overall, the close agreement in both magnitude and temporal evolution supports the reliability of the present CFD model for predicting greenhouse microclimate behavior and for comparative assessment of thermal-storage configurations. Further validation cases and related benchmarks are provided in Ref. [25].

5. Results and discussion

This section presents the transient CFD results for the greenhouse microclimate equipped with north-wall PCM thermal storage and metal-foam enhancement under hot-arid diurnal forcing. Three open-cell metal foams are considered to span practical conductivity

Table 5
Hourly boundary-condition profiles of ambient temperature and solar radiation used in the CFD simulations.

Time (h)	00	01	02	03	04	05	06	07	08	09	10	11
Ambient temperature (K)	*289*	*289*	*289*	*290*	*291*	*293*	*295*	*298*	*301*	*304*	*307*	*310*
Solar radiation ($W \bullet m^{-2}$)	*0*	*0*	*0*	*0*	*0*	*50*	*150*	*300*	*450*	*600*	*750*	*820*
Time (h)	*12*	*13*	*14*	*15*	*16*	*17*	*18*	*19*	*20*	*21*	*22*	*23*
Ambient temperature (K)	*313*	*316*	*318*	*316*	*313*	*309*	*305*	*301*	*298*	*295*	*292*	*290*
Solar radiation ($W \bullet m^{-2}$)	*850*	*830*	*780*	*650*	*500*	*350*	*200*	*80*	*0*	*0*	*0*	*0*

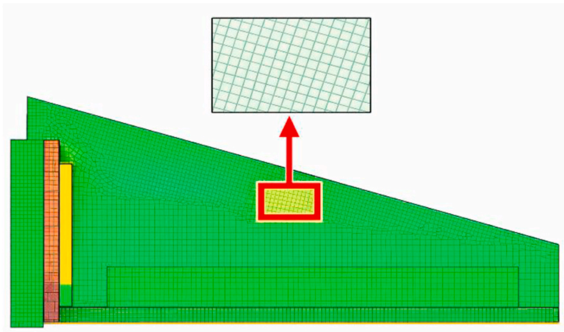

Fig. 3. Computational mesh of the greenhouse model.

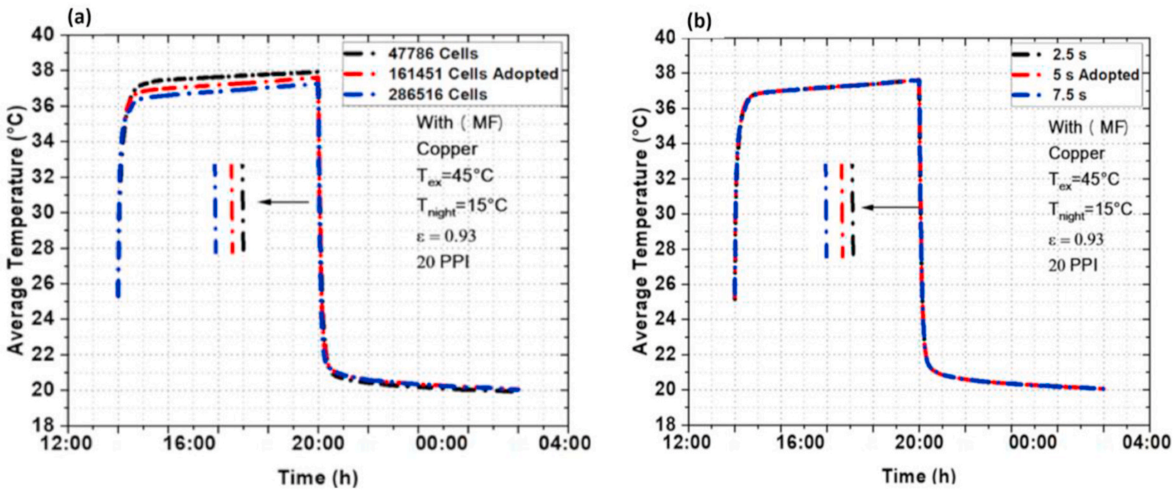

Fig. 4. (a) Mesh and (b) time-step sensitivity analysis of the volume-averaged indoor air temperature for the PCM–copper-foam greenhouse.

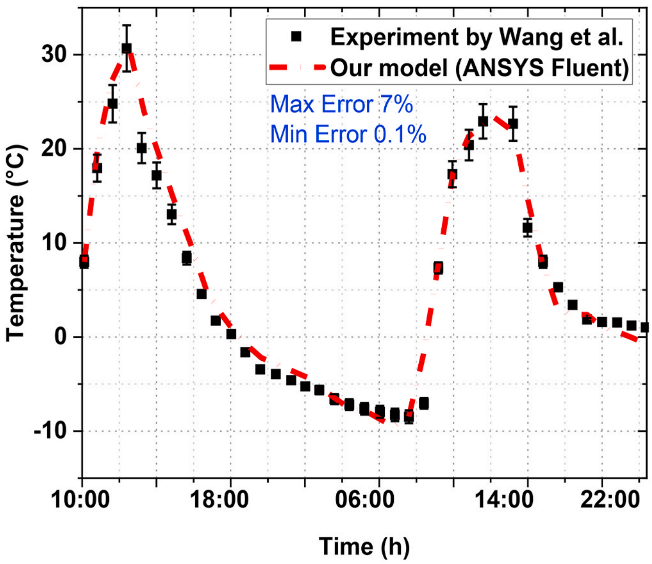

Fig. 5. Validation of the present model against experimental data from Ref. [34]: comparison of the transient indoor temperature evolution over a full diurnal cycle.

levels for heat-transfer enhancement in PCM modules: copper, aluminum, and steel, all evaluated at fixed morphology (20 PPI) and high porosity ($\varepsilon = 0.93$), along with a reference case without foam. To provide a comprehensive picture of the coupled thermo-fluid response, greenhouse temperature contours, temperature–time histories at representative monitoring locations (air, crop zone, soil, PCM, and ash brick), the evolution of the volume-averaged PCM temperature and liquid fraction during charging and discharging, and airflow structure through velocity-magnitude contours, streamlines, and line-sampled velocity profiles are reported and analyzed.

5.1. Temperature field

Fig. 6 compares the greenhouse temperature contours at t = 15000 s under different external daytime ambient temperatures (T = 289, 303, 308, 313, and 318 K) for (a) the PCM unit without MF and (b) the PCM unit filled with copper foam. The isotherms show that, without foam, a larger warm zone develops near the roof and the temperature gradients around the PCM module are more pronounced, indicating slower heat spreading inside the storage unit and weaker buffering of the indoor air. With copper foam, the temperature field becomes smoother and more uniform, and the extent of the hot region is reduced at the same time, reflecting faster internal heat redistribution within the PCM module and more effective absorption of incoming heat. Similar isotherm patterns are obtained with other MFs, meaning that the overall stratification structure remains qualitatively comparable, while the main difference lies in the level of temperature homogenization achieved.

5.2. PCM thermal response

5.2.1. Effect of metal foam type

Fig. 7 shows how the imposed daytime temperature (25–45 °C) and the presence of a MF inside the PCM unit jointly shape the daily thermal response ($T_{night} = 15$ °C, $\varepsilon = 0.93$, 20 PPI). In all subfigures, the charging period (from about 12:00 to 20:00) is characterized by a rapid temperature rise followed by a quasi-plateau: higher daytime temperatures shift the whole plateau upward, meaning the PCM is driven harder and stores more heat during the afternoon. The sharp drop around 20:00 marks the transition to night conditions. The subsequent slow decay reflects heat release from the storage unit while the system relaxes toward the night boundary condition. Comparing the four cases highlights the role of internal heat spreading. Without MF (a), the PCM experiences the largest daytime temperature levels for a given daytime temperature, indicating that heat is less uniformly redistributed inside the PCM and local

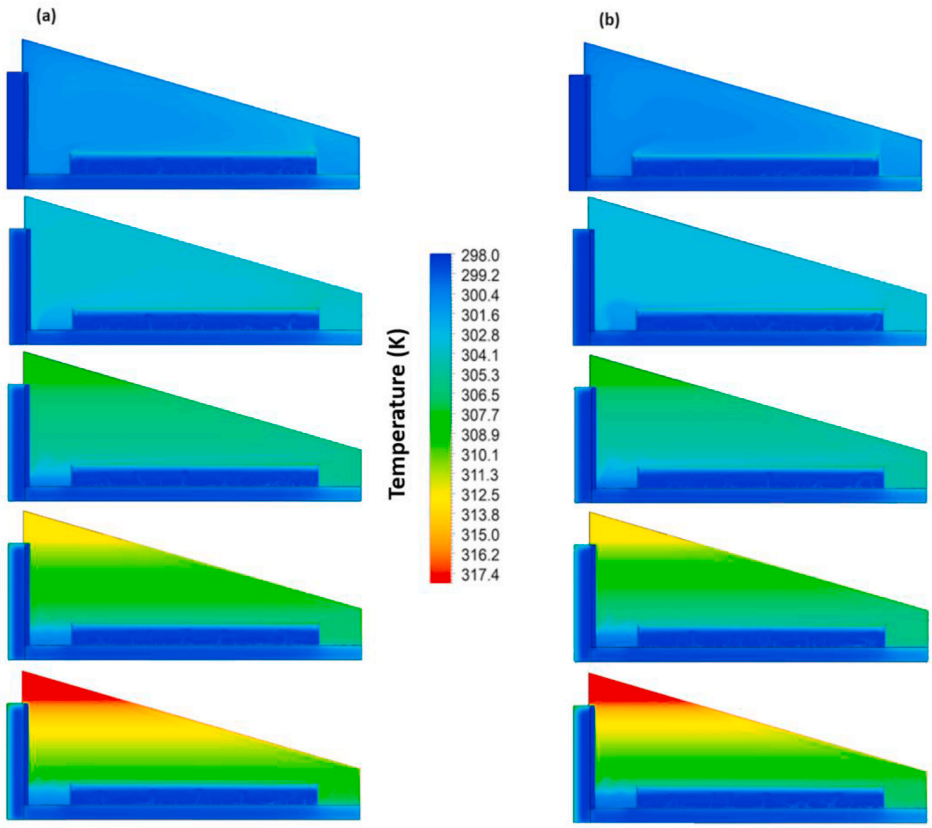

Fig. 6. Greenhouse temperature contours at t = 15000 s under external daytime ambient temperatures for (a) PCM unit without metal foam and (b) PCM unit filled with copper foam.

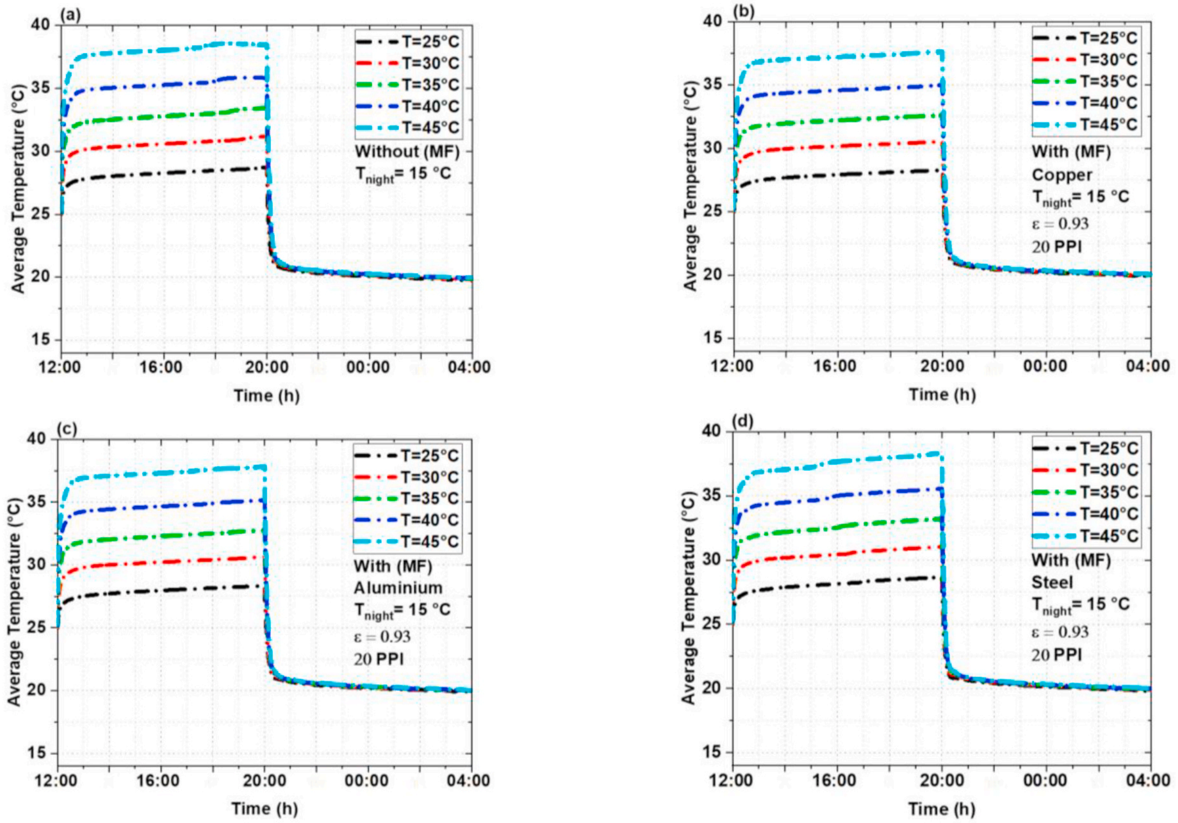

Fig. 7. Effect of daytime temperature and MF enhancement on the average PCM temperature over a day–night cycle: (a) without MF, (b) copper foam, (c) aluminum foam, and (d) steel foam.

overheating develops more easily. With MFs (b–d), the daytime plateau is reduced and the curves are smoother because the foam provides an internal conductive network that redistributes the incoming heat more effectively, so the PCM can absorb energy with less temperature build-up. The strength of this damping follows the foam conductivity: copper foam (b) gives the strongest stabilization (typically lowering the peak/plateau by about 5–7 K relative to the no-foam case), aluminum foam (c) produces an intermediate

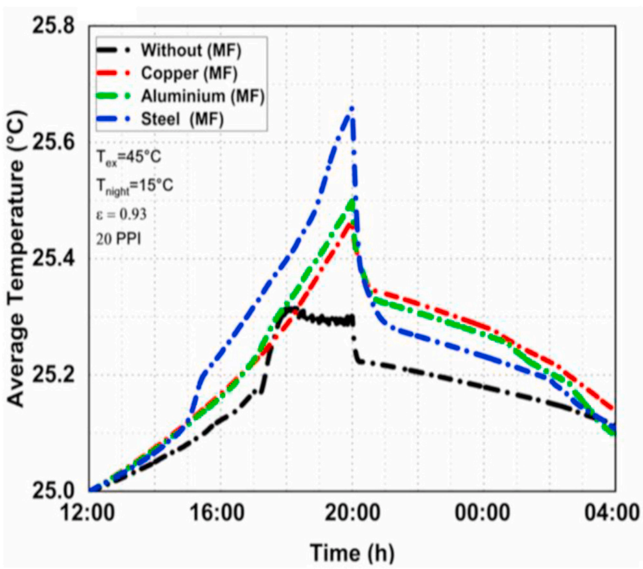

Fig. 8. Average temperature evolution of the PCM unit over a day–night cycle for the case without MF and with copper, aluminium, and steel foams.

reduction (about 3–5 K), and steel foam (d) yields the smallest improvement (about 2–3 K). After the day–night switch, the temperature trajectories become much closer across all cases because the external nighttime condition dominates the long-time behavior. However, the foam-filled cases maintain a slightly more controlled discharge response, consistent with faster internal heat redistribution and more effective use of the stored heat during the cooling period.

5.2.2. Average PCM temperature

Fig. 8 shows how the average temperature evolves over a full day–night cycle ($T_{ex} = 45$ °C during the day, $T_{night} = 15$ °C at night) for the PCM unit without MF and with 20 PPI metal foams ($\varepsilon = 0.93$). From 12:00 to about 20:00, all cases warm up, but the presence of foam makes the rise steeper and the daytime level higher. The steel-foam case reaches the highest peak just before the night transition (around 25.65–25.70 °C near 20:00), followed by aluminium (about 25.48–25.52 °C) and copper (about 25.45–25.48 °C), whereas the no-foam case stays lower and shows a plateau around 25.28–25.32 °C. Right after the day–night switch (=20:00), a sharp drop appears in every curve, marking the rapid change in boundary driving and the onset of discharge. After that, the curves decay more gradually toward early morning. The foam-filled cases remain slightly warmer than the no-foam case for most of the night (typically by a few tenths of a degree between 20:00 and 02:00), consistent with stronger heat exchange between the PCM and its surroundings: more energy is taken up during the day and then released back more effectively during the night. The pronounced overshoot seen with steel (highest peak and then a quicker fall immediately after 20:00) suggests a larger share of the daytime input appears as sensible heating compared with copper/aluminium, while copper and aluminium produce a more moderate peak and a smoother nighttime relaxation, indicating steadier charging/discharging behavior.

5.2.3. Average liquid fraction

Fig. 9 shows how the average liquid fraction of the PCM evolves over a day–night cycle for the reference case (without MF) and for PCM filled with 20 PPI metal foams ($\varepsilon = 0.93$) under $T_{ex} = 45$ °C and $T_{night} = 15$ °C. During the heating period (roughly 12:00–20:00), all cases exhibit an almost linear rise in liquid fraction, meaning the PCM progressively melts as it absorbs solar-driven heat. The presence of metal foam clearly accelerates melting and increases the melted fraction reached by the end of the daytime period. At around 20:00, the liquid fraction peaks at about 0.22 without MF, while it reaches about 0.35 with copper foam, 0.33 with aluminium foam, and 0.29 with steel foam. Compared with the no-foam configuration, this corresponds to an increase of roughly 0.13 for copper, 0.11 for aluminium, and 0.07 for steel, showing that higher-conductivity foams promote faster internal heat spreading and make a larger portion of the PCM participate in phase change within the available daytime window. After the onset of night cooling (after 20:00), the liquid fraction decreases in all cases, indicating solidification and heat release to the greenhouse. The foam-assisted cases remain above the no-foam curve throughout the cooling period, indicating greater daytime melting and a larger liquid fraction retained into the night. This trend follows the same ranking across all cases: copper provides the strongest enhancement, followed by aluminum and then steel. The persistence of this ranking is consistent with the ability of each foam to reduce internal thermal resistance and improve heat spreading within the PCM, thereby promoting more effective charging and a more sustained discharge.

5.2.4. Effect of monitoring location

Fig. 10 tracks the diurnal thermal response at several monitoring points when the PCM unit is filled with copper foam. Across all panels, the curves show a clear “day–night” transition: a rapid warming and quasi-plateau during the daytime heating period (roughly the first half of the cycle), followed by a sharp drop at the onset of night cooling and then a slow relaxation. In Fig. 10(a), the indoor-air

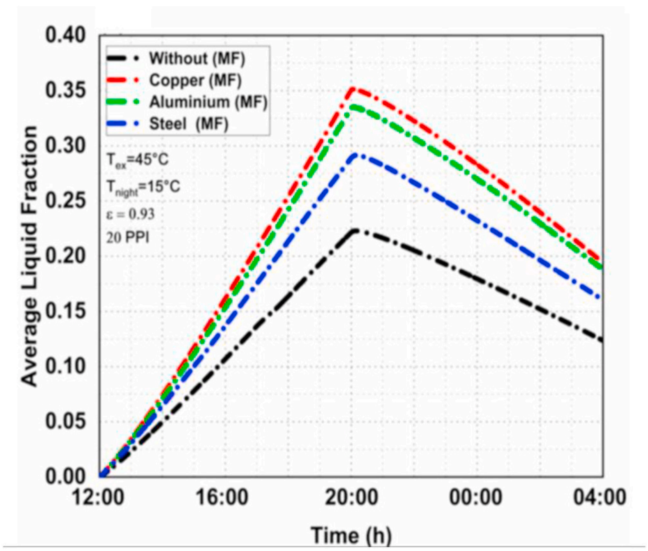

Fig. 9. Average PCM liquid fraction during a day–night cycle for the case without MF and with 20 PPI copper, aluminium, and steel foams.

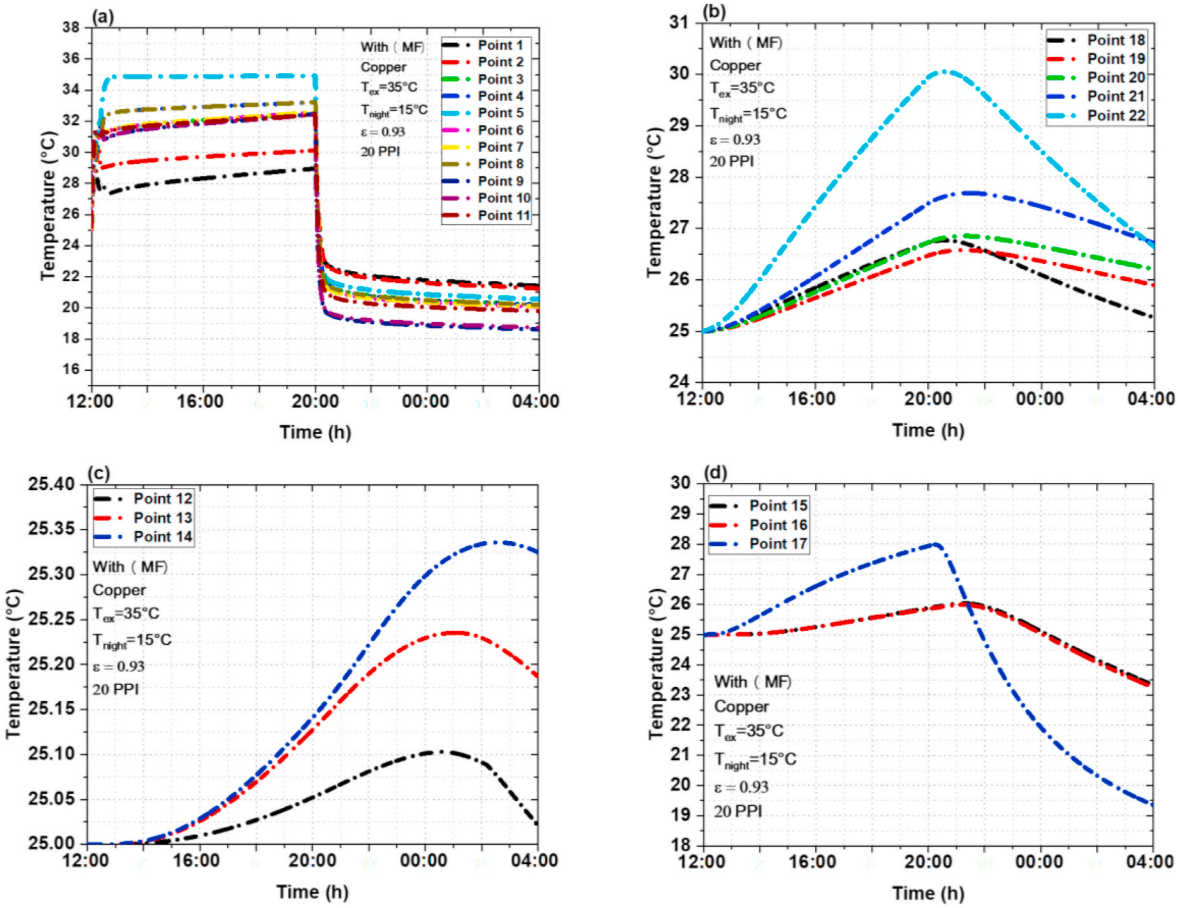

Fig. 10. Temperature evolution at monitoring points with copper-foam-filled PCM storage: (a) indoor air, (b) ground, (c) PCM, and (d) ash brick.

points (1–11) rise quickly at the beginning of the day and then evolve more gradually, which is typical of a greenhouse where solar gains dominate early and the thermal mass progressively damps the transient. During the daytime plateau, the spread between locations remains limited (the highest indoor point stays only on the order of a few to several degrees above the lowest one), indicating that the air field is relatively well mixed while still preserving some stratification. After the night transition, all indoor points collapse toward a narrow band, showing that the internal temperature becomes more uniform once the external forcing is removed and the system is governed mainly by heat release from the storage and losses to the surroundings. Fig. 10(b) highlights a stronger spatial contrast in the ground temperatures (points 18–22). The curves exhibit a delayed response and a pronounced hump, with peak values occurring later than the indoor air. This lag is consistent with the higher thermal inertia of the soil and the fact that heat reaches deeper layers by conduction. The peak-to-peak separation between ground points is noticeably larger than in the indoor air, reflecting a persistent vertical gradient in the substrate. During the night period, the ground cools more slowly than the air, which helps sustain the near-floor temperature and reduces the risk of sharp nighttime drops. The PCM temperatures in Fig. 10(c) (points 12–14) increase smoothly during the day and remain more clustered than the ground signals, which indicates efficient internal heat spreading within the storage unit. The remaining gap between PCM points (typically only a few degrees at most near the peak) reflects internal gradients across the PCM volume, but their limited magnitude supports the role of copper foam in improving thermal uniformity inside the module. After sunset, the PCM curves decrease gradually, consistent with the stored heat being released over an extended period rather than being lost rapidly. Finally, Fig. 10(d) shows the ash-brick temperatures (points 15–17), which follow the day–night cycle but with moderated slopes compared with the indoor air. One location responds more strongly and then cools faster after the night transition, suggesting proximity to a boundary exposed to stronger heat exchange, while the other points remain more buffered. Taken together, the four panels indicate that the copper foam improves thermal coupling between the PCM and its surroundings, limiting local hot spots during charging and providing a smoother, more sustained thermal release during the cooling phase. Similar trends are expected with other foams, while copper typically delivers the strongest damping because its higher conductivity reduces internal PCM thermal resistance.

5.3. Airflow response

5.3.1. Velocity-field evolution with daytime temperature

Fig. 11 illustrates the evolution of the velocity field inside the greenhouse and around the PCM unit at four instants (t = 1000, 15000, 28000, and 40000 s) for five daytime temperatures: (a) 298 K, (b) 303 K, (c) 308 K, (d) 313 K, and (e) 318 K. For all cases, the airflow is primarily buoyancy-driven and progressively develops into a dominant recirculation loop within the greenhouse. At the early stage (t = 1000 s), the motion is still forming, with low velocities mainly confined near the boundaries and small localized vortices close to the PCM module. By t = 15000 s, a well-defined circulation cell occupies most of the upper greenhouse region, while secondary eddies appear near the floor and around the PCM enclosure, indicating enhanced local mixing and heat exchange. As time increases to t = 28000 and 40000 s, the flow becomes more organized and stronger, with a pronounced high-velocity pathway along the inclined roof and a return stream toward the opposite side, which improves convective transport across the greenhouse volume. The effect of daytime temperature is clear and systematic. Increasing the daytime temperature from 298 K to 318 K intensifies buoyancy forces, leading to higher peak velocities and a wider high-speed zone, especially in the upper region and along the roof. At 298 K, the velocity levels remain relatively modest even at later times, whereas at 318 K the circulation strengthens substantially and the high-velocity layer extends further downstream, reflecting more vigorous natural convection. Inside the PCM unit, velocities remain comparatively small due to confinement and flow resistance, yet the surrounding airflow increases markedly with temperature, enhancing the external convective renewal near the PCM surface and promoting faster redistribution of heat within the greenhouse. Overall, Fig. 11 confirms the transition from a developing natural-convection regime (t = 1000 s) to a quasi-established circulation (t = 15000–40000 s), with the strength and spatial extent of airflow strongly amplified as the daytime temperature rises.

5.3.2. Velocity profiles along analysis lines

Fig. 12 compares velocity profiles along two sampling lines (line 1 and 3) at $T_{ex} = 30\ ^{\circ}C$ and $T_{night} = 15\ ^{\circ}C$ for the PCM unit without foam and with copper, aluminium, and steel foams ($\varepsilon = 0.93$, 20 PPI). in all casesl, inserting MF changes how heat is redistributed inside the PCM module, which modifies the buoyancy forcing around it and reshapes the natural-convection circulation inside the greenhouse. The impact is therefore seen both in the peak velocities and, more importantly, in how uniform or localized the airflow becomes. Along Line 1 (panel a), the copper- and aluminium-foam cases keep a relatively higher and smoother velocity level through the main part of the domain, with a broad region around 0.10–0.11 m/s. In the no-foam case, the profile shows a clearer mid-domain weakening, with a wider low-velocity zone dropping to roughly 0.03–0.04 m/s, which suggests a larger stagnant region when internal heat spreading in the storage unit is weaker. The steel-foam case typically lies between these trends, improving circulation compared with no foam but remaining less uniform than copper/aluminium. The narrow spikes near the extremities are consistent with local acceleration in boundary or high-shear regions, whereas the differences over the middle portion reflect how each foam affects the overall convective driving. Along Line 3 (panel b), the velocity exhibits a two-zone behavior: a higher level near the start of the line (about 0.12–0.13 m/s), followed by a minimum near the middle (around x = 0.6 m), then a second rise downstream. Copper and aluminium lead to a moderate but sustained downstream recovery, with secondary peaks around 0.07–0.08 m/s. The no-foam case remains slightly lower downstream (near 0.06 m/s). Steel shows the most localized downstream intensification, reaching about 0.13–0.14 m/s close to the end of the line, indicating a more concentrated buoyancy plume rather than a broadly distributed circulation.

6. Conclusion

This paper presents a transient CFD study of passive thermal regulation in a south-facing greenhouse operating under hot-arid diurnal conditions, using north-wall PCM storage enhanced with open-cell MFs. Three foam skeleton materials were considered to span practical conductivity levels for PCM heat-transfer enhancement: copper, aluminum, and steel, all evaluated at fixed morphology (20 PPI) and high porosity ($\varepsilon = 0.93$), alongside a reference case without foam. The main conclusions are as follows:

(1) A coupled 2D transient CFD microclimate model was developed and validated against published greenhouse measurements, capturing the diurnal temperature evolution and the timing of extrema with good agreement, and with the largest deviations confined to short intervals during steep transients.
(2) MF insertion significantly improves heat spreading inside the PCM modules, producing smoother temperature fields, reduced local overheating during daytime charging, and a more effective use of the PCM volume for latent storage compared with the no-foam configuration.
(3) Foam material strongly controls the enhancement level. The stabilization follows the thermal-conductivity ranking, with copper providing the largest reduction in daytime PCM peak or plateau temperatures (about 5–7 K relative to no foam), aluminum yielding an intermediate reduction (about 3–5 K), and steel producing the smallest improvement (about 2–3 K).
(4) Foam enhancement accelerates melting and increases latent-heat utilization within the available daytime window. Under the examined cycle (Tex = 45 °C, Tnight = 15 °C), the maximum daily liquid fraction increases from about 0.22 (no foam) to about 0.35 (copper), 0.33 (aluminum), and 0.29 (steel, indicating greater daytime melting and a larger liquid fraction retained into the night.
(5) Airflow remains primarily buoyancy-driven and evolves toward a dominant recirculation loop. Improved thermal coupling between the storage module and the surrounding air modifies buoyancy forcing, reduces stagnant regions, and promotes more uniform circulation, with copper and aluminum generally supporting smoother velocity distributions than steel.

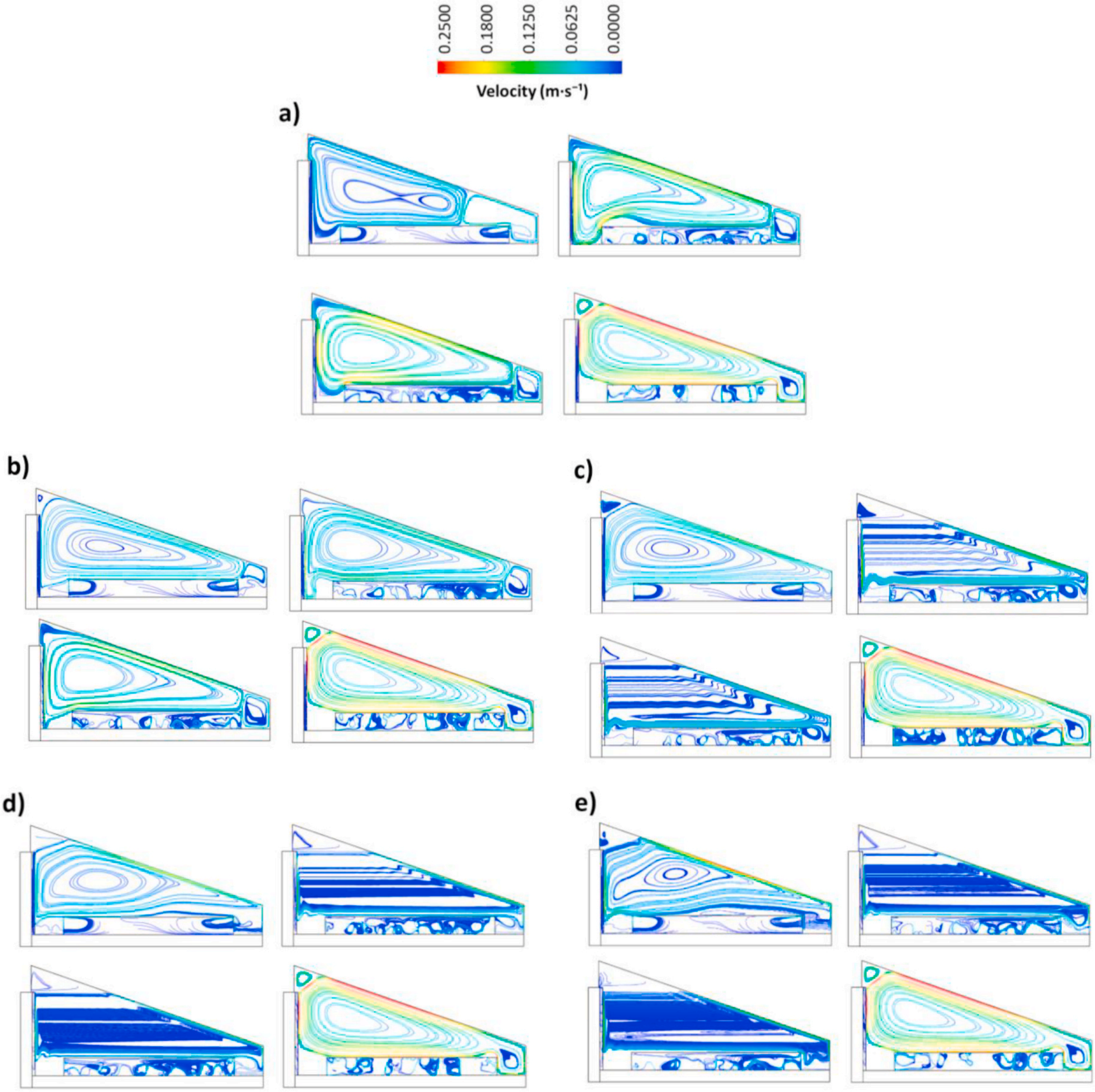

Fig. 11. Velocity magnitude contours and streamlines in the greenhouse–PCM system for daytime temperatures (a) 298 K, (b) 303 K, (c) 308 K, (d) 313 K, and (e) 318 K.

The present study adopts several simplifying assumptions. The analysis is two-dimensional, thermo-physical properties are treated as constant within each phase, and the PCM–foam composite is modeled under a local thermal equilibrium assumption using mixture-effective properties. In addition, thermal contact resistance between wall layers is neglected after a sensitivity check, and only one greenhouse geometry, foam morphology (20 PPI, $\varepsilon = 0.93$), and representative diurnal boundary-condition profile are considered. These choices are appropriate for the comparative, material-level objective addressed here, but future work should extend the investigation to 3D effects, broader foam morphologies (PPI, porosity, thickness), different PCM melting ranges, and multi-day cycling. Coupling the CFD framework with optimization and techno-economic assessment would further support systematic selection of foam material and storage configuration to maximize microclimate stability and minimize energy demand under realistic climatic and operational constraints.

CRediT authorship contribution statement

Samir Gouga: Validation, Supervision, Software, Resources, Conceptualization. **Atef Chibani:** Software, Resources, Formal analysis, Conceptualization. **Kamel Mesmoudi:** Formal analysis, Data curation, Conceptualization. **Farhan Lafta Rashid:** Visualization, Validation, Supervision, Software. **Zaki Mrzog Alaofi:** Project administration, Methodology, Investigation, Conceptualization.

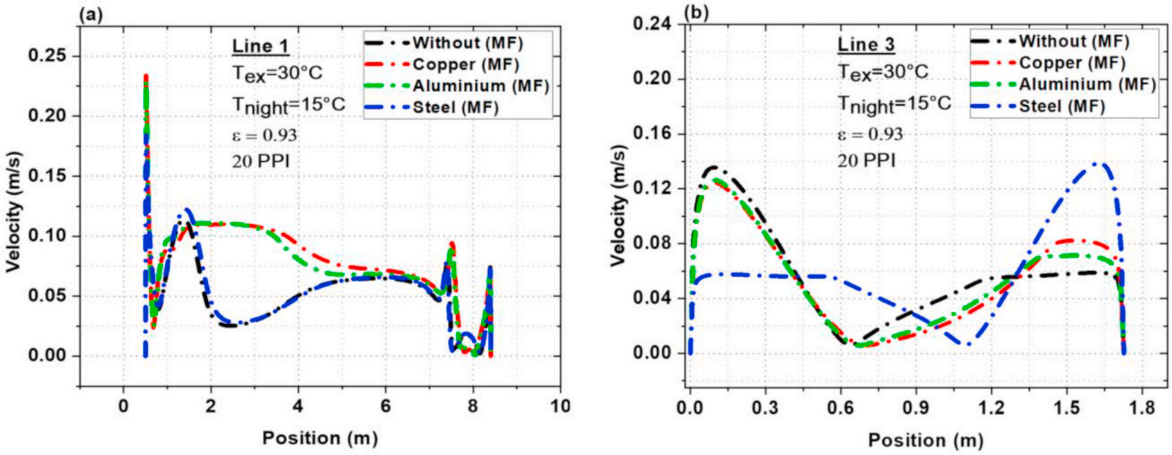

Fig. 12. Velocity distribution along (a) Line 1 and (b) Line 3 for the PCM unit without MF and with copper, aluminium, and steel foams.

Yazen M. Alawaideh: Writing – review & editing, Writing – original draft, Validation, Supervision. **Tasneem Alayed:** Writing – review & editing, Writing – original draft, Visualization, Software. **Mohamed kezzar:** Writing – original draft, Project administration, Methodology, Formal analysis, Data curation. **Mohamed Rafik Sari:** Writing – original draft, Project administration, Methodology, Formal analysis, Data curation. **Ibrahim Mahariq:** Resources, Project administration, Methodology, Conceptualization. **Aya M. Al-Zuheiri:** Software, Resources, Project administration, Methodology, Investigation. **Ioan-Lucian Popa:** Software, Resources, Project administration.

Declaration of competing interest

The authors declare that they have no known competing financial interests or personal relationships that could have appeared to influence the work reported in this paper.

Acknowledgments

The authors extend their appreciation to the Deanship of Research and Graduate Studies at King Khalid University for funding this work through Large Research Project under grant number RGP2/217/46.

Data availability

Data will be made available on request.

References

[1] J. Spinoni, et al., How will the progressive global increase of arid areas affect population and land-use in the 21st century, Global Planet. Change 205 (2021) 103597, https://doi.org/10.1016/j.gloplacha.2021.103597.
[2] O. Abedrabboh, M. Koç, Y. Biçer, Sustainable food development for societies in hot arid regions: thermoeconomic assessment of passive-cooled soil-based and hydroponic greenhouses, J. Clean. Prod. 412 (2023) 137250, https://doi.org/10.1016/j.jclepro.2023.137250.
[3] A.K. Hussein, et al., A review of the application of hybrid nanofluids in solar still energy systems and guidelines for future prospects, Sol. Energy 272 (2024) 112485, https://doi.org/10.1016/j.solener.2024.112485.
[4] N.S. Dhaidan, et al., Enhancing the thermal performance of an agricultural solar greenhouse by geothermal energy using an earth-air heat exchanger system: a review, Geothermics 123 (2024) 103115, https://doi.org/10.1016/j.geothermics.2024.103115.
[5] N. Choab, A. Allouhi, A. El Maakoul, T. Kousksou, S. Saadeddine, A. Jamil, Review on greenhouse microclimate and application: design parameters, thermal modeling and simulation, climate controlling technologies, Sol. Energy 191 (2019) 109–137, https://doi.org/10.1016/j.solener.2019.08.042.
[6] M.S. Ahamed, H. Guo, K. Tanino, Energy saving techniques for reducing the heating cost of conventional greenhouses, Biosyst. Eng. 178 (2019) 9–33, https://doi.org/10.1016/j.biosystemseng.2018.10.017.
[7] O. Abedrabboh, M. Koç, Y. Biçer, Modelling and analysis of a renewable energy-driven climate-controlled sustainable greenhouse for hot and arid climates, Energy Convers. Manag. 273 (2022) 116412, https://doi.org/10.1016/j.enconman.2022.116412.
[8] H. Jouhara, A. Żabnieńska-Góra, N. Khordehgah, D. Ahmad, T. Lipinski, Latent thermal energy storage technologies and applications: a review, Int. J. Thermofluids 5–6 (2020) 100039, https://doi.org/10.1016/j.ijft.2020.100039.
[9] P. Piché, et al., Design, construction and analysis of a thermal energy storage system adapted to greenhouse cultivation in isolated northern communities, Sol. Energy 204 (2020) 90–105, https://doi.org/10.1016/j.solener.2020.04.008.
[10] P. Amoatey, Influence of Phase Change Materials on Thermal Comfort , Greenhouse Gas Emissions , and Potential Indoor Air Quality Issues Across Different Climatic Regions : a Critical Review, 2022, pp. 1–35, https://doi.org/10.1002/er.8734. August.
[11] F. Iachachene, Z. Haddad, E. Abu-Nada, M.A. Sheremet, Natural convection melting of phase change material in corrugated porous cavities, Sustain. Energy Technol. Assessments 53 (2022) 102734, https://doi.org/10.1016/j.seta.2022.102734.
[12] J. Zhu, X. Zhang, W. Hua, J. Ji, X. Lv, Current status and development of research on phase change materials in agricultural greenhouses: a review, J. Energy Storage 66 (2023) 107104, https://doi.org/10.1016/j.est.2023.107104.

[13] F.L. Rashid, et al., Enhancing solar greenhouse efficiency through the integration of phase change materials: thermal regulation and sustainable crop growth, Energy Build. 337 (2025) 115667, https://doi.org/10.1016/j.enbuild.2025.115667.
[14] K. Huang, T. Mi, C. Zheng, L. Wang, X. Yi, Development of a novel composite phase change material based on paints and brick for energy storage applications in agricultural greenhouses, J. Energy Storage 89 (2024) 111734, https://doi.org/10.1016/j.est.2024.111734.
[15] A. Badji, et al., Experimental assessment of a greenhouse with and without PCM thermal storage energy and prediction their thermal behavior using machine learning algorithms, J. Energy Storage 71 (2023) 108133, https://doi.org/10.1016/j.est.2023.108133.
[16] P. Llorach-Massana, J. Peña, J. Rieradevall, J.I. Montero, Analysis of the technical, environmental and economic potential of phase change materials (PCM) for root zone heating in Mediterranean greenhouses, Renew. Energy 103 (2017) 570–581, https://doi.org/10.1016/j.renene.2016.11.040.
[17] A.S. Sedighi, R. Roshandel, Integration of phase change materials for energy efficiency in agriculture greenhouses, J. Energy Storage 134 (2025) 118180, https://doi.org/10.1016/j.est.2025.118180.
[18] Y. Guan, Q. Meng, T. Ji, W. Hu, W. Li, T. Liu, Experimental study of the thermal characteristics of a heat storage wall with micro-heat pipe array (MHPA) and PCM in solar greenhouse, Energy 264 (2023) 126183, https://doi.org/10.1016/j.energy.2022.126183.
[19] E. Meng, et al., Experimental study on thermal performance of high absorption latent heat storage plate (LHSP) in greenhouse, Int. Commun. Heat Mass Tran. 149 (2023) 107150, https://doi.org/10.1016/j.icheatmasstransfer.2023.107150.
[20] N. Zhang, X. Pan, Z. Zhang, Y. Yuan, M. Sultan, S. Attia, Carbonated balsa-based shape-stable phase change materials with photothermal conversion and application in greenhouse, Sol. Energy Mater. Sol. Cells 266 (2024) 112699, https://doi.org/10.1016/j.solmat.2024.112699.
[21] Q.O. Ogunlowo, et al., Energy- and yield-based performance evaluation of a phase change material–integrated single-span double-layered with a thermal screen greenhouse, Therm. Sci. Eng. Prog. 50 (2024) 102499, https://doi.org/10.1016/j.tsep.2024.102499.
[22] H. Cheradi, Z. Haddad, F. Iachachene, K. Mansouri, M. Arıcı, A comprehensive numerical study on melting performance in a storage cavity with partial metal foam integration: design and economic assessment, J. Energy Storage 85 (2024) 110985, https://doi.org/10.1016/j.est.2024.110985.
[23] A. Chibani, Z. Haddad, M. Boukraa, T. Chekifi, F.L. Rashid, Optimizing solidification for efficient heat discharge in LHTES systems: foam architecture and cooling-wall design, Int. Commun. Heat Mass Tran. 169 (2025) 109807, https://doi.org/10.1016/j.icheatmasstransfer.2025.109807.
[24] A. Chibani, Z. Haddad, M. Boukraa, T. Chekifi, Metal foam-enhanced latent heat storage: role of pore density and directional heating on heat transfer performance, J. Energy Storage 143 (2026) 119542, https://doi.org/10.1016/j.est.2025.119542.
[25] S. Gouga, et al., Greenhouse microclimate regulation with metal-foam-assisted phase-change storage: a numerical investigation, J. Energy Storage 143 (2026) 119636, https://doi.org/10.1016/j.est.2025.119636.
[26] H. Bouhoun Ali, P.E. Bournet, V. Danjou, C. Migeon, CFD analysis of the climate inside a closed greenhouse at night including condensation and crop transpiration, Acta Hortic. (1170) (Jul. 2017) 53–60, https://doi.org/10.17660/ActaHortic.2017.1170.5.
[27] O. Kolditz, Author and Glenn LA , Reviewer, Computational methods in environmental fluid mechanics, Appl. Mech. Rev. 55 (6) (Oct. 2002) B117–B118, https://doi.org/10.1115/1.1508157.
[28] W. Jiao, Q. Liu, L. Gao, K. Liu, R. Shi, N. Ta, Computational fluid dynamics-based simulation of Crop canopy temperature and humidity in double-film solar greenhouse, J. Sens. 2020 (1) (Jan. 2020) 8874468, https://doi.org/10.1155/2020/8874468.
[29] A. Mohamed, M. Amina, S. Nassim, H.Z.J.N.-T. Science, Rayeilgh number effect on the turbulent heat transfer within a parallelepiped cavity 15 (suppl. 2) (2011) 341–356.
[30] F. Iachachene, Z. Haddad, M. Arıcı, E. Abu-Nada, M.A. Sheremet, The effect of nano encapsulated phase change materials and nanoparticles on turbulent heat transport: a conical diffuser scenario, J. Energy Storage 52 (2022) 104703, https://doi.org/10.1016/j.est.2022.104703.
[31] M. Córdova, B. Stoffel, Comparison of Various Turbulence Models in Respect to Their Suitability for CFD Calculations of Diffuser Flows, May 2006, pp. 1343–1353, https://doi.org/10.1115/GT2006-90524.
[32] M. Lateb, C. Masson, T. Stathopoulos, C. Bédard, Comparison of various types of k–ε models for pollutant emissions around a two-building configuration, J. Wind Eng. Ind. Aerod. 115 (2013) 9–21, https://doi.org/10.1016/j.jweia.2013.01.001.
[33] T. Bouhal, et al., Parametric CFD analysis and impact of PCM intrinsic parameters on melting process inside enclosure integrating fins: solar building applications, J. Build. Eng. 20 (2018) 634–646, https://doi.org/10.1016/j.jobe.2018.09.016.
[34] W.P. Wang Yuxin Liu Shuang, S. Guangying, Application effect of greenhouse root Zone thermal environment control System with latent functionally thermal fluid, Trans. Chin. Soc. Agric. Mach. 47 (8) (2016) 294, https://doi.org/10.6041/j.issn.1000-1298.2016.08.039.